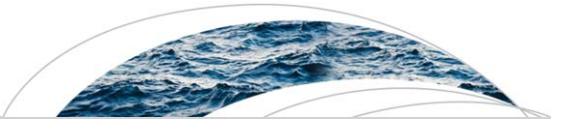
AGU PUBLICATIONS

Water Resources Research



RESEARCH ARTICLE

10.1002/2017WR021034

Remote Detection of Saline Intrusion in a Coastal Aquifer Using Borehole Measurements of Self-Potential

DJ. MacAllister[1,2,3], M. D. Jackson[1], A. P. Butler[2], and J. Vinogradov[1,4]

[1]Department of Earth Science and Engineering, Imperial College London, London, UK, [2]Department of Civil and Environmental Engineering, Imperial College London, London, UK, [3]Now at British Geological Survey, Lyell Centre, Edinburgh, UK, [4]Now at School of Engineering, King's College, University of Aberdeen, Aberdeen, UK

Key Points:
- SP data obtained from a monitoring borehole in the coastal UK Chalk aquifer display a persistent gradient with depth, and temporal variations with an ocean tidal power spectrum, caused by the movement of a saline front in close proximity to, but not intersecting, the base of the borehole
- The spatial and temporal variations in borehole SP are dominated by the exclusion-diffusion potential arising from concentration gradients across the remote saline front
- Borehole SP monitoring can be used to monitor remotely the movement of a saline front in coastal aquifers

Correspondence to:
DJ. MacAllister,
donmac@bgs.ac.uk

Citation:
MacAllister, DJ., Jackson, M. D., Butler, A. P., & Vinogradov, J. (2018). Remote detection of saline intrusion in a coastal aquifer using borehole measurements of self-potential. *Water Resources Research*, *54*. https://doi.org/10.1002/2017WR021034

Received 1 MAY 2017
Accepted 14 FEB 2018
Accepted article online 16 FEB 2018
Corrected 31 MAR 2018

This article was corrected on 31 MAR 2018. See the end of the full text for details.

Abstract Two years of self-potential (SP) measurements were made in a monitoring borehole in the coastal UK Chalk aquifer. The borehole SP data showed a persistent gradient with depth, and temporal variations with a tidal power spectrum consistent with ocean tides. No gradient with depth was observed at a second coastal monitoring borehole ca. 1 km further inland, and no gradient or tidal power spectrum were observed at an inland site ca. 80 km from the coast. Numerical modeling suggests that the SP gradient recorded in the coastal monitoring borehole is dominated by the exclusion-diffusion potential, which arises from the concentration gradient across a saline front in close proximity to, but not intersecting, the base of the borehole. No such saline front is present at the two other monitoring sites. Modeling further suggests that the ocean tidal SP response in the borehole, measured prior to breakthrough of saline water, is dominated by the exclusion-diffusion potential across the saline front, and that the SP fluctuations are due to the tidal movement of the remote front. The electrokinetic potential, caused by changes in hydraulic head across the tide, is one order of magnitude too small to explain the observed SP data. The results suggest that in coastal aquifers, the exclusion-diffusion potential plays a dominant role in borehole SP when a saline front is nearby. The SP gradient with depth indicates the close proximity of the saline front to the borehole and changes in SP at the borehole reflect changes in the location of the saline front. Thus, SP monitoring can be used to facilitate more proactive management of abstraction and saline intrusion in coastal aquifers.

Plain Language Summary Self-potential (SP) measurements in coastal boreholes respond to the movement of seawater, which occurs remotely from the borehole. Thus, monitoring changes in SP in coastal boreholes could assist the management of abstraction of fresh water from coastal aquifers.

1. Introduction

Seawater intrusion is a global phenomenon occurring in many coastal aquifers (van Weert et al., 2009; Werner et al., 2013). Reduction in recharge to aquifers and/or the abstraction of groundwater decreases the freshwater hydraulic head and can result in the saline front advancing inland toward abstraction boreholes (van Weert et al., 2009). On the south-coast of the UK, seawater intrusion is considered one of the main risks to the Chalk aquifer groundwater resource (Jones & Robins, 1999). The Chalk is a dual porosity aquifer; without secondary fracture porosity, the Chalk would not be a productive water resource. However, these fracture networks also control the extent of saline intrusion, providing highly permeable pathways for rapid movement of seawater into the aquifer (Jones & Robins, 1999; Robins & Dance, 2003). High-resolution monitoring methods, that provide spatial and temporal information on the movement of the saline front, are required for improved management of coastal abstractions. Surface geophysical methods, such as electrical resistivity tomography (ERT) and electromagnetic methods (EM) can provide the required resolution (de Franco et al., 2009; Werner et al., 2013). However, such methods can be difficult to conduct in many areas where surface infrastructure or other restrictions prevent access. Furthermore, and despite recent advances, ERT and EM provide information only about the saturated rock resistivity rather than directly about the aquifer fluid dynamics, although they can serve as a useful proxy for the latter when saturation changes occur in an unconfined aquifer or when natural or artificial tracers are present (de Franco et al., 2009; Falgàs et al., 2009; Rosas-Carbajal et al., 2013). Borehole ERT and EM can also be conducted, but require instrumentation to be installed within the saline zone. Moreover, downhole ERT requires a minimum of two boreholes.

© 2018. The Authors.
This is an open access article under the terms of the Creative Commons Attribution-NonCommercial-NoDerivs License, which permits use and distribution in any medium, provided the original work is properly cited, the use is non-commercial and no modifications or adaptations are made.

Recent evidence suggests that measurements of borehole self-potential (SP) could be used to monitor seawater intrusion in real time, using an array of electrodes permanently installed in a single monitoring borehole some distance from the saline front (MacAllister et al., 2016). SP arises in order to maintain overall electrical neutrality when a separation of charge occurs due to gradients in pressure (electrokinetic potential) and concentration (electro-exclusion-diffusion potential or simply exclusion-diffusion potential) (e.g., Glover et al., 2012; Revil, 1999). The electrokinetic potential (EK) arises in response to pressure gradients induced by tides and during abstraction. Concentration gradients are a characteristic feature of seawater intrusion and also give rise to an electro-exclusion-diffusion potential (EED). The measured SP is the electrical potential difference (i.e., voltage) between two or more electrodes within the monitoring array.

SP monitoring has been demonstrated in a variety of hydrological settings (e.g., Jackson et al., 2012a; Jardani et al., 2006; Kullessa et al., 2003; Revil et al., 2005; Revil et al., 2009). A number of laboratory experiments and numerical modeling studies have suggested that a remote saline front could be detected using SP measurements (Ikard et al., 2012; Jackson et al., 2012b; Jardani et al., 2013; Maineult et al., 2004, 2005; Martinez-Pagan et al., 2010). However, only two previous studies have obtained SP data in coastal aquifers and neither was designed to provide information on the location or movement of a remote saline front (Kang et al., 2014; Pezard et al., 2009).

In this study, SP data were acquired and analyzed from a coastal monitoring borehole which had low and uniform salinity for a period of at least 1 year prior to the beginning of the monitoring experiment. No significant changes in salinity were observed in the monitoring borehole until approximately 3 months into the experiment, after which the concentrations in the borehole increased, suggesting that the saline front was located close to the borehole throughout the monitoring period. Since there was little evidence of borehole processes that could have influenced the SP observed in the first 3 months, these conditions were ideal for testing the feasibility of long-term remote SP monitoring of seawater intrusion.

This study builds on recent work, using data obtained at the same boreholes in the UK Chalk aquifer, showing that time-varying pressure and concentration gradients, driven primarily by ocean tides, cause fluctuations in borehole SP with a tidal power spectrum (MacAllister et al., 2016). The aim of the work reported here is to determine the relative contribution of EED and EK potentials to the tidal SP response observed in the previous study, and determine whether borehole SP measurements, obtained using a permanently installed array of electrodes, indicate the proximity and movement of a remote saline front.

2. Methods

2.1. Field Site Description and Data Acquisition

The site locations and monitoring boreholes used in this study are shown in Figures 1a and 1b. At all sites, borehole SP monitoring was conducted within the Seaford and Lewes Nodular Chalk formations (Bristow et al., 1997). Much of the field data analyzed here were previously reported by MacAllister et al. (2016) and electrode naming conventions follow those used in that study. Monitoring and borehole profiling were conducted over a 2 year period in the Saltdean monitoring borehole (MBH) near Brighton (Figure 1b). Monitoring was undertaken using a permanently installed array of electrodes and pressure/temperature/fluid electrical conductivity (P/T/FEC) probes (Figure 1c). Borehole profiles were conducted using an electrode (BH1-C) attached to a P/T/FEC probe, both of which were detached from the main electrode array and could be moved up and down the borehole (the traveling electrode (TER), Figure 1c). Data from the Saltdean MBH are the main focus of this study, but we make some comparisons with data obtained at the nearby Balsdean MBH which is approximately 1 km further inland (Figure 1b), and also at a monitoring borehole at an inland site approximately 80 km from the coast (denoted by the square in Figure 1a). In all boreholes voltage measurements from the electrodes were recorded relative to a reference electrode in the borehole, just below the water table (electrode BH13-C in the case of the Saltdean MBH; Figure 1c) (MacAllister et al., 2016). Locating the reference electrode below the water table eliminates surface noise and complex SP responses in the unsaturated zone (MacAllister et al., 2016; Maineult et al., 2008). All boreholes were open hole, with 10–20 m sections of casing in the unconsolidated chalk. The casing in the Saltdean MBH was stainless steel and the borehole was ca. 0.5 m diameter. The other two boreholes used PVC casing and were ca. 0.14 m diameter.

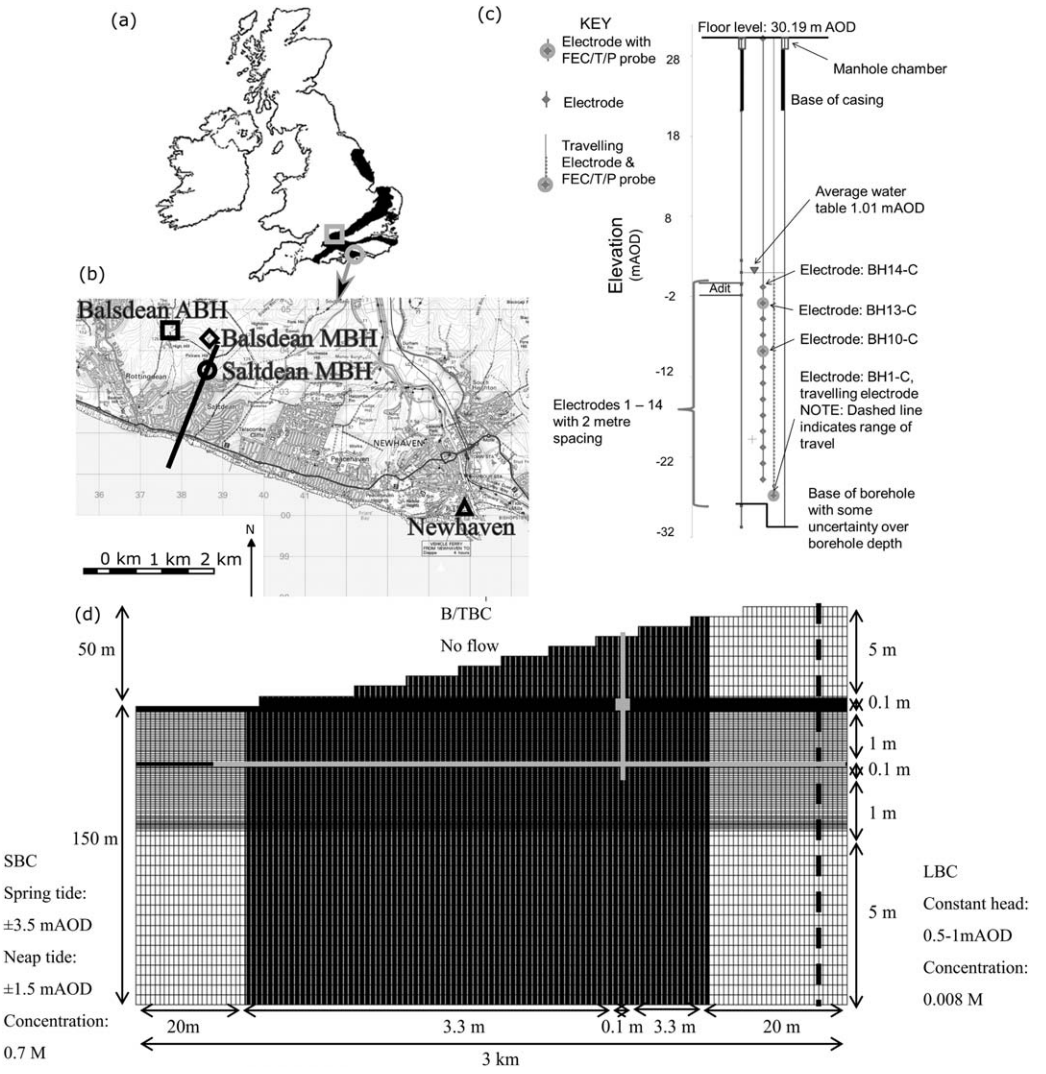


Figure 1. (a) Location of the coastal (hollow gray circle) and inland (hollow gray square) SP monitoring sites. The black areas indicate the UK Chalk aquifer. (b) Location of the coastal Saltdean MBH (hollow circle), Balsdean MBH (hollow diamond), Balsdean ABH, (hollow square), and the Newhaven tidal gauge (hollow triangle). The black line illustrates the 2-D model section. (c) Saltdean MBH SP monitoring array. Depths are in mAOD. (d) Numerical model grid. The thick black dashed line indicates the model extent used for the electrodynamic model. The vertical gray line shows the position of the Saltdean MBH, the horizontal gray line shows the position of the modeled fracture zone and the gray rectangle shows the position of a possible adit. SBC denotes seaward boundary conditions, LBC landward boundary conditions and B/TBC bottom and top boundary conditions. The arrows illustrate cell and domain sizes. Adapted from MacAllister et al. (2016). Maps: © Crown copyright and database rights 2015 Ordnance Survey (Digimap License).

2.2. Numerical Models

Simple two-dimensional (2-D) models of the coastal aquifer were constructed along the section shown in Figure 1b. The models were used to investigate the source mechanisms giving rise to the SP signal at the Saltdean MBH during monitoring periods when there was no saline water present in the borehole. A number of coupled hydrodynamic, and solute transport models were constructed. The outputs of these (pressure and salt concentration) were used to calculate the electrodynamic properties of the aquifer. The electrodynamic model was used to determine the relative contributions of the EED and EK potentials to the measured SP. The simple two-dimensional models were not designed to simulate exactly the hydrodynamic and electrodynamic properties of the aquifer, but rather to investigate the relative magnitudes of the SP source mechanisms related to ocean tidal processes in the aquifer. The models serve as a starting point to understand the SP signals in the complex and heterogeneous coastal UK Chalk aquifer.

2.2.1. Hydrodynamic Model

The coupled hydrodynamic and solute transport models were solved using Eclipse 100 (Schlumberger, 2010), a fully implicit, three-phase, variable density flow simulator. Eclipse 100 uses a finite-difference, finite-volume scheme to solve for pressure, concentration, and saturation and has previously been used to model seawater intrusion (Labregère, 2006). The dual porosity system in the aquifer was not explicitly modeled; rather, an equivalent porous medium (EPM) approach was used (Berkowitz et al., 1988; Ireson & Butler, 2013; Long et al., 1982; Singhal & Gupta, 2010). The effects of recharge to the aquifer were approximated by varying the inland head boundary condition, based on observations reported in Jones and Robins (1999). This is a reasonable first-order representation of the influence of recharge on the modeled pressure gradients, which, along with the concentration gradients, are the key output required from the hydrodynamic model. Pumping at the Balsdean abstraction borehole (ABH) was also neglected, because tidal fluctuations at Saltdean were significantly larger than pumping effects (Figures 2b and 2c).

Salt transport was simulated in Eclipse 100 using:

$$\frac{\partial}{\partial t}(S_w C_M) = \frac{k_w}{\mu_w}(\nabla P_w - \rho_w g z) C_M + Q_w C_M \quad (1)$$

Here S_w is the water saturation (dimensionless), C_M is the salt concentration as total ionic strength (M), k_w is the saturation-dependent intrinsic permeability to water (m^2), μ_w is the dynamic viscosity of water (Pa s), P_w is the water pressure (Pa), ρ_w is the water density which varies linearly with salinity (kg/m^3), g is the gravitational acceleration (m/s^2), z is the depth (m), and Q_w is a source/sink term denoting gains/losses of water to/from the aquifer (m^3/s). The equation is solved in Eclipse 100 using the Newton iteration method.

The salt was modeled as total concentration and advection was assumed to dominate salt transport. This assumption is a reasonable first-order approximation in the UK Chalk aquifer (Cook et al., 2012) because the Chalk is often considered to demonstrate subkarstic behavior (Banks et al., 1995; Maurice et al., 2006). The Saltdean MBH is located within a high permeability zone below a dry valley (Jones & Robins, 1999; Robins & Dance, 2003), and the modeled section approximately follows the profile of this valley. The inland boundary was placed at the base of the interfluve, 2.5 km from the coast. The model domain and grid, which was most refined around the monitoring borehole and a fracture zone, less refined in the areas surrounding these features and coarsest at the extremities of the model, are shown in Figure 1d. An outline of the hydrodynamic model properties follows (summarized in Table 1). The boundary conditions are shown in Figure 1d. Note that in Figure 1d, the position of a suspected adit is also shown. The properties of this possible adit are highly uncertain. Therefore, it was assessed, and is discussed below, separately.

In the UK Chalk aquifer, most of the flow occurs within fractures, so the kinematic porosity and bulk hydraulic conductivity, both of which are primarily provided by the fractures, were modeled (Table 1). The bulk hydraulic conductivity in the bottom 100 m of the model was decreased to account for the reduction in hydraulic conductivity at depth within the Chalk aquifer (Allen et al., 1997; Jones & Robins, 1999; Williams et al., 2006). It was assumed that flow 50 m below the water table was negligible because fractures are closed owing to the rock overburden or the presence of secondary calcite (Allen et al., 1997; Jones & Robins, 1999; Price, 1987; Williams et al., 2006). The bulk hydraulic conductivity of the Chalk was modeled as isotropic (Price, 1987) which is a reasonable first-order assumption due to the presence of orthogonal, solution-enhanced fracture sets and relatively few marl seams at this location (Bristow et al., 1997; Jones & Robins, 1999; Maurice et al., 2012).

Although the aquifer was primarily modeled as an EPM, a fracture zone was included at the base of the Saltdean MBH based on evidence from borehole logs (Jones & Robins, 1999). It was assumed that this fracture zone is ca. 30 cm wide (Bloomfield, 1996; Maurice et al., 2006; Worthington, 2015; Worthington & Ford, 2009) and that individual fractures contributed an additional 1% to the kinematic porosity, relative to the bulk rock, within the fracture zone (Owen & Robinson, 1978; Price, 1987). Due to convergence problems, the borehole was not included in the hydrodynamic models.

The simulations were conducted in three stages. First, a steady state saline wedge was developed. The model was initially filled with seawater below the water table, which was set at 0 m above ordnance datum (mAOD), and freshwater was injected from the inland boundary at constant head. The unsaturated zone filled with water immediately, owing to the small pore throat radius and corresponding high air-entry

pressure in the Chalk (Price, 1987) (Table 1). Next, tidal forcing was added by perturbing the steady state head at the seawater boundary such that a new dynamic equilibrium was obtained, defined by a consistent average position of the saline front within the fracture zone. Finally, the model was run for a single spring/neap cycle.

In the first of these stages, the midtidal level (0 mAOD) was used as the seaward boundary. For the subsequent steps, tidal fluctuations were modeled using a fluctuating head boundary based on tidal gauge data (Figure 1b). The boundary comprised two overlapping sine functions, one with a 12.42 h period replicating the dominant tidal component and the other with a 2 week period for the spring/neap tidal cycle. The maximum amplitude for the tidal function used in the models was 3.5 m. The inland head was set at 1 mAOD to match water levels during the summer months when recharge is low.

For the final spring/neap model runs, the boundary conditions (Figure 1d) were changed to ensure that the saline front moved toward the monitoring borehole. Thus, the inland head was dropped to 0.5 mAOD, allowing investigation of severe drought conditions (Jones & Robins, 1999) when the movement of the saline front is most significant.

2.2.2. Electrodynamic Model

The electrodynamic and hydrodynamic problems are related as follows (Gulamali et al., 2011; Jackson et al., 2012b; Leinov & Jackson, 2014; Revil, 1999; Sill, 1983):

$$j = -\sigma_{rec}\nabla V + L_{EK}\nabla(P_w - \rho_w g h) + L_{EED}\nabla \ln(\sigma_{fec}) \tag{2}$$

Here j is the current density (A m^{-2}), σ_{rec} is the electrical conductivity of the saturated rock (S/m), σ_{fec} is the FEC (S/m), ∇V is the electric potential gradient (V/m), $\nabla(P - \rho_w g h)$ is the pressure gradient above hydrostatic pressure (Pa/m) (density varies with salinity and temperature) and $\nabla \ln(\sigma_{fec})$ is the gradient of the natural log of FEC ((S/m) m^{-1}). The FEC of the water was used as a proxy for activity (Revil, 1999) because FEC was measured in the field. Revil (1999) originally used FEC as a proxy for a 1:1 electrolyte. Here however, the measured FEC accounts for all ions dissolved in solution so it serves as a first-order approximation for the more complex natural electrolytes in the coastal aquifer. The terms L_{EK} (A Pa^{-1} m^{-1}) and L_{EED} (A (S/m) m^{-1}) are the electrokinetic and electro-exclusion-diffusion cross-coupling terms, respectively. Assuming there are no external current sources or sinks, charge conservation yields:

$$\nabla \cdot \boldsymbol{j} = 0 \tag{3}$$

Combining equations (2) and (3) yields the equation solved in the electrodynamic model:

$$\nabla \cdot \sigma_{rec}\nabla V = \nabla \cdot (L_{EK}\nabla(P_w - \rho_w g h) + L_{EED}\nabla \ln(\sigma_{fec})) \tag{4}$$

At all boundaries we set $\nabla V = 0$ and $\nabla(P_w - \rho_w g h) = \nabla \ln(\sigma_{fec}) = 0$. The electrodynamic problem was solved using a control-volume finite-difference method (Recktenwald, 2012) based on the scheme developed by Saunders et al. (2008) and extended by Gulamali et al. (2011), Jackson et al. (2012b), and Ijioma and Jackson (2014).

The cross-coupling terms are expressed in terms of the saturated rock electrical conductivity (σ_{rec}) and by a coupling coefficient (C_x) (Jackson, 2015):

$$L_x = \sigma_{rec} C_x \tag{5}$$

The coupling coefficients relate the magnitude of the SP gradient to the associated gradient in fluid potential or concentration and were measured in the laboratory (Leinov et al., 2010; Leinov & Jackson, 2014; Vinogradov et al., 2010).

Major ions were measured in the laboratory using ion chromatography and these results were used to estimate total dissolved solids (TDS) and ionic strength (C_M) of both groundwater and seawater (Table 1). TDS was then converted to FEC using a conversion factor of 0.7, which approximates the FEC of seawater and carbonate-rich groundwater (Walton, 1989). The FEC (σ_{fec}) was then corrected for temperature (Hayashi, 2004):

$$\sigma_{fec} = \sigma_{f_{spec}}(1 + 0.02(T - 298.15)) \tag{6}$$

Here $\sigma_{f_{spec}}$ is the specific fluid electrical conductivity (S/m) of the water at 298.15 K (25°C) and T is the average measured temperature (K) which was 284.45 K (11.3°C). The temperature was very stable for the duration of the monitoring experiment with a standard deviation of 0.1 K. It was not possible to obtain ERT or

EM measurements over the domain due to access issues (Figure 1b). Thus, the electrical conductivity of the rock in the domain was calculated using Archie's law (Telford et al., 1990):

$$\sigma_{rec} = \phi^m \sigma_{fec} \tag{7}$$

Here ϕ is porosity, m is the dimensionless cementation exponent of the rock, and σ_{fec} is obtained from the hydrodynamic model. Despite the limitations associated with Archie's law in carbonates (Barker, 1994), its use here provided a reasonable match to the measured rock conductivity in the seawater dominated regime (measured in the laboratory following the method outlined in Vinogradov et al., 2010), but slightly underestimated the measured rock conductivity in the freshwater regime (see Table 1 for measured and modeled values). Due to the high air-entry pressure (Table 1), the unsaturated zone remained fully water saturated (Price, 1987) so there was no need to model the saturation dependence of the rock electrical conductivity. In the electrodynamic model, the porosity used in Archie's law was the mean Chalk porosity in East Sussex (Table 1) because the bulk rock is the main pathway for current flow.

The EK coupling coefficients (Table 1) in groundwater and seawater were obtained from laboratory measurements on chalk samples following the method described in Vinogradov et al. (2010) and modeled using equation (8), where C_M is the total ionic strength (M) of the water. Equation (8) gives an EK response consistent with that observed in a pumping test in the UK Chalk aquifer (Jackson et al., 2012a). Since the electrode array is installed below the water table vertical infiltration, from rainfall, does not contribute to the observed EK (MacAllister et al., 2016), which further justifies the use of a variable inland head boundary condition as a proxy for recharge:

$$C_{EK} = -0.0071 C_M^{-0.908} \tag{8}$$

The EED coupling coefficient, based on the equations presented in Leinov and Jackson (2014) and Jackson (2015), was scaled from the exclusion potential end-member using the laboratory measured EED potential (V_{mEED}, Table 1). The EED potential was measured following the method described in Leinov and Jackson (2014). The modeled coupling coefficient was (Appendix A):

$$C_{EED} = -S_{EED} \frac{k_b T}{e} \tag{9}$$

Here k_b is Boltzmann's constant (1.38×10^{-23} J/K), e is electron charge (1.602×10^{-19} C), and S_{EED} is a scaling factor (Table 1). The laboratory experiments used natural seawater and groundwater so we implicitly account for the complexity of these natural waters in the models. All modeled voltages are reported with reference to the voltage at a location in the model similar to the position of the reference electrode in the Saltdean MBH (Figure 1d). As a result of the linearity of the potential fields, the SP is simply the sum of the modeled EED and EK potentials. All equations are developed here using SI units, but in the results and discussion sections, and in Table 1, more convenient units are used.

2.2.3. Sensitivity Analysis

The model described above matched the data most closely. However, basic sensitivity analysis was conducted, to investigate the uncertainties associated with the hydrodynamic and electrodynamic model properties.

The impact of model permeability was assessed in two ways. First, the bulk hydraulic conductivity of the top 100 m of the model was varied across the range shown in Table 1. The change in extent and shape of the saltwater wedge was minimal. Second, the permeability in the chalk is known to decrease with depth. Thus, the permeability in the bottom 100 m of the model domain was modeled in two ways. The first approach, highlighted above, assumed flow was negligible. The second approach assumed that fractures contribute to flow in the deeper zone, which changed the shape and position of the saline front. Inland head also controlled the geometry of the saline front. Thus, two end-members for the inland head were tested; 3 mAOD during periods of high rainfall and 1 mAOD during the summer months when rainfall is lower (Jones & Robins, 1999).

The key electrodynamic properties investigated during the sensitivity analysis were the bulk rock conductivity and the SP coupling coefficients. These were investigated by varying the parameter values across the ranges reported in Table 1, in order to investigate the impact of the laboratory measurement uncertainty on the modeled SP.

Table 1
Model Properties, Ranges Indicate Sensitivity Analysis.

Symbol	Description	Value	Unit	Source
Hydrodynamic Model Properties				
C_M	Groundwater concentration	0.008	M	Measured in laboratory
C_M	Seawater concentration	0.70	M	Measured in laboratory
μ_w	Groundwater dynamic viscosity	0.0011359	kg/m s	Labregère et al. (2006)
μ_w	Seawater dynamic viscosity	0.0011360	kg/m s	Labregère et al. (2006)
ρ_w	Groundwater density	1,000	kg/m^3	N/A
ρ_w	Seawater density	1,025	kg/m^3	N/A
B	Rock compressibility	1×10^{-10}	Pa^{-1}	Mathias (2005)
B	Groundwater compressibility	4.885×10^{-10}	Pa^{-1}	Labregère et al. (2006)
B	Seawater compressibility	4.875×10^{-10}	Pa^{-1}	Labregère et al. (2006)
ϕ_k	Bulk kinematic porosity	0.01	N/A	Butler et al. (2012)
ϕ_k	Fracture kinematic porosity	0.02	N/A	Butler et al. (2012)
k_w (*K*)	Bulk intrinsic permeability (Bulk hydraulic conductivity)	1.5×10^{-11} to 3.9×10^{-11} (10–40)	m^2 (m/d)	Price (1987) and MacDonald and Allen (2001)
k_w (*K*)	Fracture intrinsic permeability (Fracture hydraulic conductivity)	1.6×10^{-9} to 6.4×10^{-9} (1600 – 65000)	m^2 (m/d)	Price (1987)
P	Air-entry pressure	$29x10^4$	Pa	Price (1987)
Electrodynamic Model Properties				
Φ	Bulk rock porosity	0.4	N/A	Bloomfield et al. (1995)
Φ	Fracture porosity	0.41	N/A	Butler et al. (2012)
M	Cementation factor	2.4	N/A	Measured in laboratory
σ_{rec}	Rock electrical conductivity seawater	5.2–5.75 (5.2 measured)	mS/cm	Measured in laboratory
σ_{rec}	Rock electrical conductivity groundwater	0.06–0.25 (0.25 measured)	mS/cm	Measured in laboratory
C_{EK}	EK coupling coefficient groundwater	-0.575 ± 0.080	mV/mH_2O	Measured in laboratory
C_{EK}	EK coupling coefficient seawater	-0.0101 ± 0.0020	mV/mH_2O	Measured in laboratory
V_{mEED}	Measured EED potential	22.60 ± 8.62	mV	Measured in laboratory
S_{EED}	EED scaling factor	-0.13 to -0.25	N/A	Calculated from laboratory results

Note. Hydraulic conductivity (K) is shown for convenience in brackets.

3. Results

3.1. Field Monitoring Results

Borehole referenced SP and FEC, collected by MacAllister et al. (2016), are shown in Figure 2 for the duration of the monitoring experiment. Saline breakthrough, caused by a gradual decline in the inland head, occurred in September 2013 and 2014. SP data acquired during this period were not included in the modeling reported below, which only used data acquired when the saline front was remote from the borehole. SP was anticorrelated with head (Figures 2b and 2c) which is consistent with an EK source mechanism for SP with an ocean tidal power spectrum. However, an initial analysis by MacAllister et al. (2016) suggested that EK cannot be solely responsible for the ocean tidal spectrum within the SP. This is investigated further below.

SP also became more negative with depth with a gradient of ca. 0.22 mV/m (Figures 3a and 3b). Only the Saltdean borehole displayed a gradient with depth (Figure 3a). During saline breakthrough in July 2013 the gradient recorded by the permanent array decreased (Figure 2). However, comparison with the gradient recorded by the traveling electrode (TER, BH1-C) after the breakthrough event, revealed that the decrease was an electrode artifact (Figure 3b) caused by the changes in salinity at the electrodes (Jougnot & Linde, 2013).

Conductivity remained low and relatively constant in the borehole before and after the saline breakthrough events observed each October (Figures 3c and 3d). However, conductivity profiles conducted during saline breakthrough revealed that vertical flow occurred in the borehole across the tidal cycle (Figures 3e and 3f). Saline water entered via the fracture zone at the base of the borehole and flowed up the borehole during a rising tide and vice versa when the tide was falling. These tidally induced vertical flows likely also occurred throughout the rest of the monitoring period. The numerical models described above were used to investigate the relative contributions of EK and EED potentials to the observed SP prior to any saline breakthrough occurring in the borehole. Saline breakthrough caused processes which complicated the interpretation of the SP

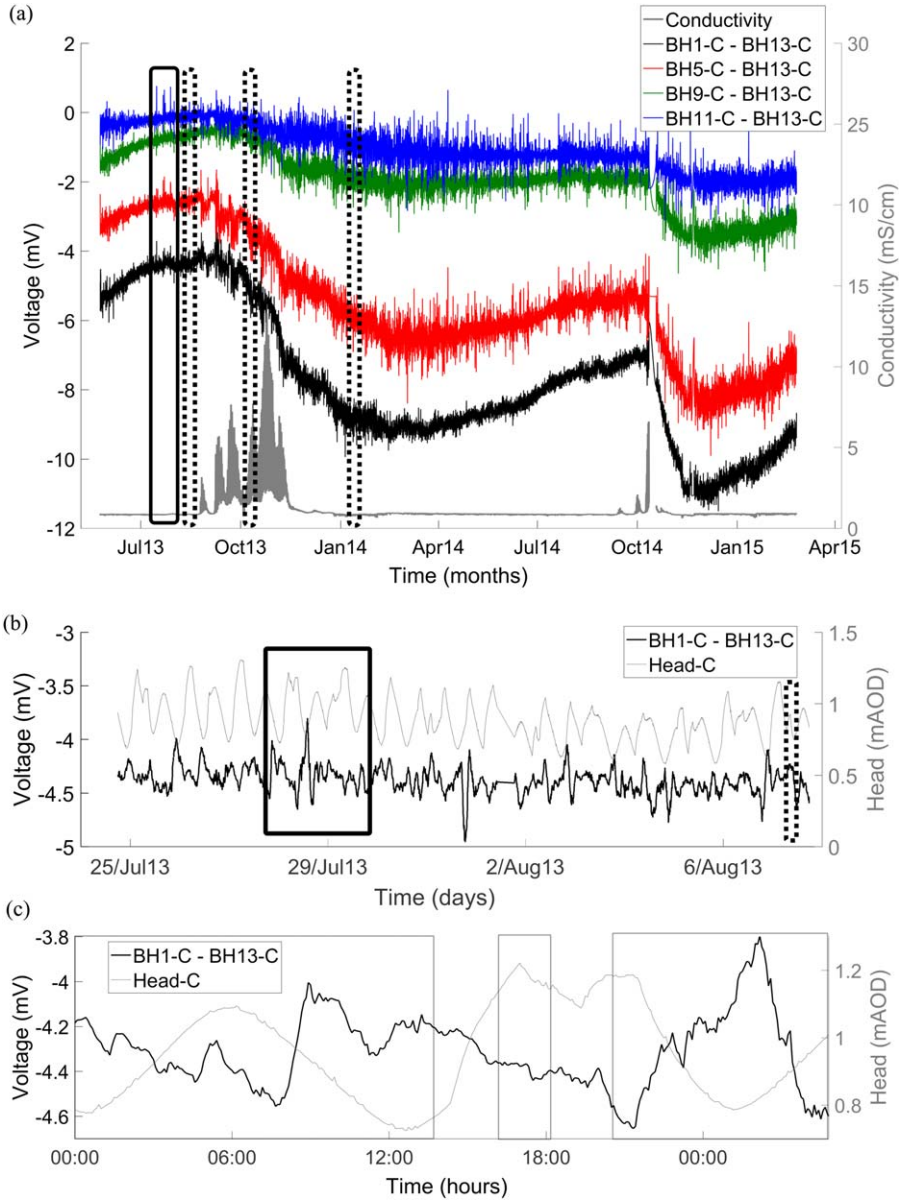


Figure 2. (a) Borehole referenced SP data at the Saltdean MBH smoothed with a 2 h window. The voltage becomes more negative with depth (i.e., from BH11-C to BH1-C). (b) Borehole referenced SP zoomed on July to August 2013. In Figures 2a and 2b, the solid black boxes highlight the time period used to test the models, before saline water entered the borehole, and the dashed black boxes highlight the times that spot profiles of SP and/or FEC were obtained. The spot profiles are presented in Figure 3. (c) Borehole referenced SP zoomed on 28 July 2013, despite the noise it is clear that the SP signal is anticorrelated with the head. The gray boxes indicate periods when the Balsdean ABH was pumped at ca. 600 m^3/h. There is a clear pumping signal in the Saltdean MBH head data at around 18:00, where changes in slope occurred in response to changes in pumping in the Balsdean ABH, but the tidal signature is significantly larger. The head response at the Saltdean MBH lagged changes in pumping at the Balsdean ABH by 2–3 h.

(Figure 3b); postbreakthrough data are presented here for transparency, but are not of interest in the context of remote monitoring of the saline front, so the modeling focused on the period prior to saline breakthrough.

3.2. Modeling Results

In order to identify the main hydrodynamic and electrodynamic contributions to the observed SP, a large number of models were constructed. However, only a few of these models showed a reasonable match to the data. The results reported here are drawn from the model that provided the best match. Figure 4 shows contour plots of the modeled FEC and SP distribution during a spring tide. Broadening of the FEC contours

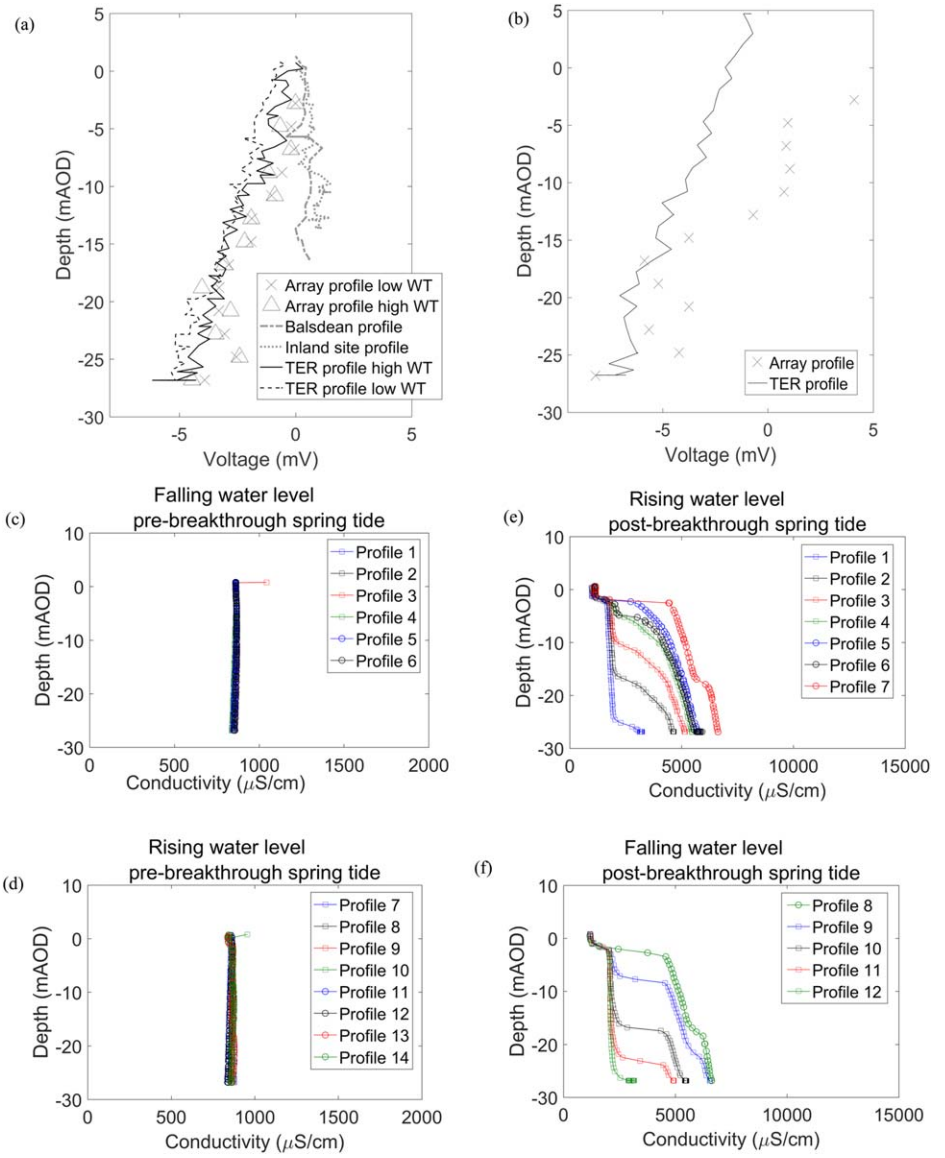


Figure 3. (a) Normalized SP data at the Saltdean MBH for high and low water tables (WT) on 8 August 2013 compared to SP recorded in the Balsdean MBH on 17 November 2015 and SP at the inland site on 16 July 2013. (b) Normalized SP at the Saltdean MBH from the permanent array and TER on 6 February 2014. The gradient recorded by the permanent array decreased after saline breakthrough. Profiles were normalized by subtracting the shallowest value from the rest of the profile. (c and d) FEC profiles in the Saltdean MBH on 8 August 2013 prior to saline breakthrough. (e and f) FEC profiles in the Saltdean MBH on 10 October 2013 during saline breakthrough revealed that vertical flow occurs within the borehole.

in parts of the model domain (Figure 4a) is likely caused by the dominance of advection and/or different cell sizes in the model grid.

The modeled pressure fluctuations provide a reasonable fit to the observed fluctuations (Figure 5a). Simulated conductivity was slightly lower than observed (600 μS/cm against 800 μS/cm) but the fluctuations were the same order of magnitude and very small (Figure 5b). As discussed previously pumping at the Balsdean ABH (Figure 1b) was not included in the models, explaining the slight discrepancy in the shape of the observed and simulated results. All of the model hydrodynamic results are obtained from the same position as the field data (BH1-C), and simulated voltages are presented with reference to a position equivalent to the field reference electrode (BH13-C) (Figure 1c).

Figure 4b shows a contour plot of the SP distribution during a spring tide. The saline front was initially only ca. 4 m from the base of the borehole. The modeled fracture zone was necessary to reproduce the field

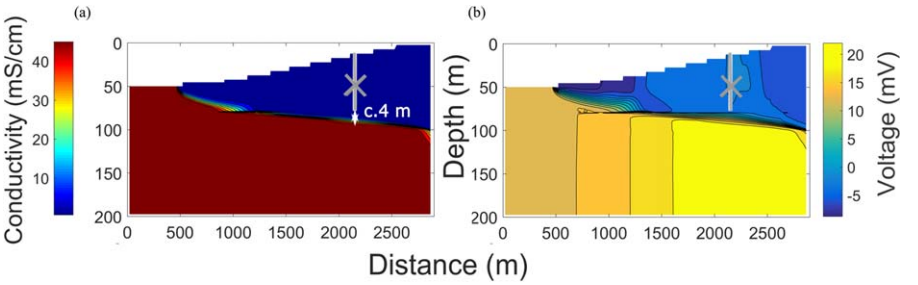


Figure 4. (a and b) FEC and SP for the model which best matched the observed data. This model had a low inland head boundary condition and low bulk permeability at the base. The gray line marks the position and extent of the borehole in the field (the borehole is not explicitly represented in the hydrodynamic model). The gray cross represents the position of the reference voltage in the model, equivalent to the position of the reference electrode in the field (Figure 1). The distance from the base of the borehole to the midpoint of the saline front is indicated.

observations. The zone introduced both a high permeability pathway for movement of the saline front and a high electrical conductivity pathway for current flow.

The model replicated the magnitude of the observed SP data reasonably well (Figure 5c). The modeled SP was anticorrelated with pressure (Figure 6a). EK contributed only ca. 20 μV to the tidal SP (Figures 6a and 6b). The EK response was expected to be 180° out of phase with the pressure fluctuation but it was ca. 90°

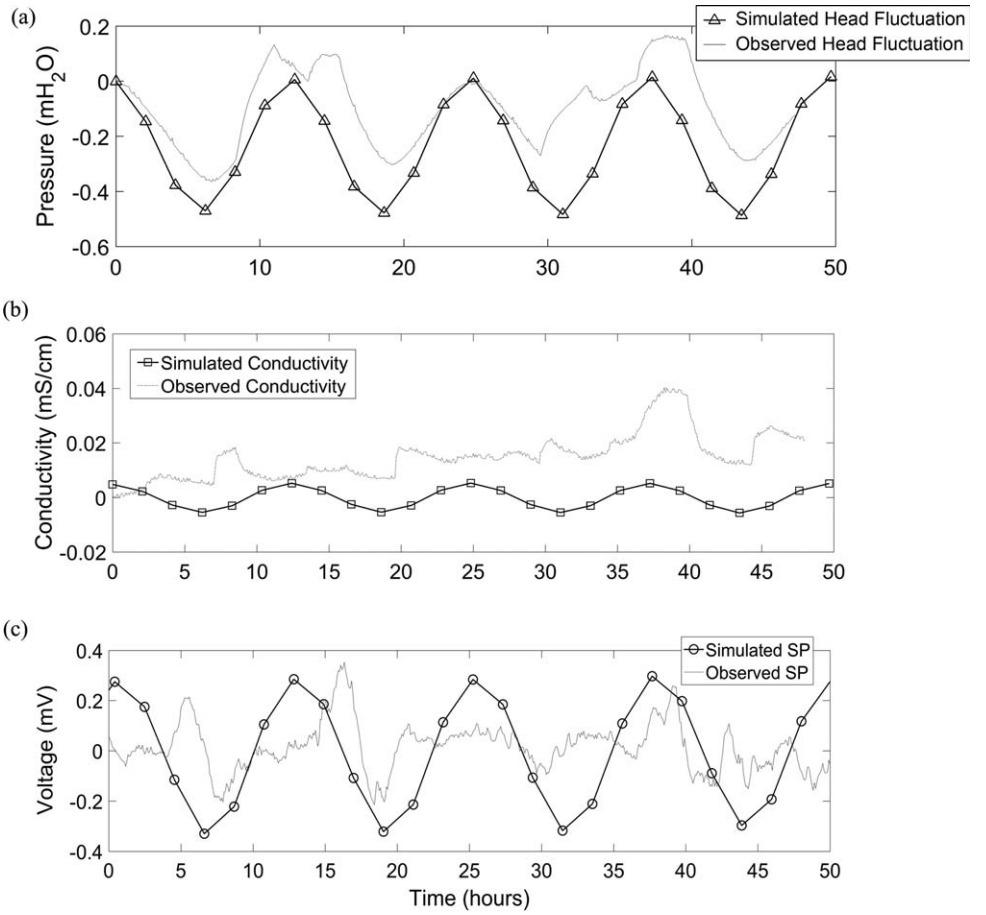


Figure 5. Modeled time series results. Observed data were recorded at BH1-C and were from the period beginning 28 July 2013, which is highlighted by the solid black boxes in Figure 2. (a) Simulated versus observed pressure fluctuation. (b) Simulated versus observed FEC. (c) Simulated versus observed SP. Simulated SP is the sum of the simulated EK and EED potential contributions. All observed and simulated data were normalized by subtracting the initial value from each data set from the remainder of the time series.

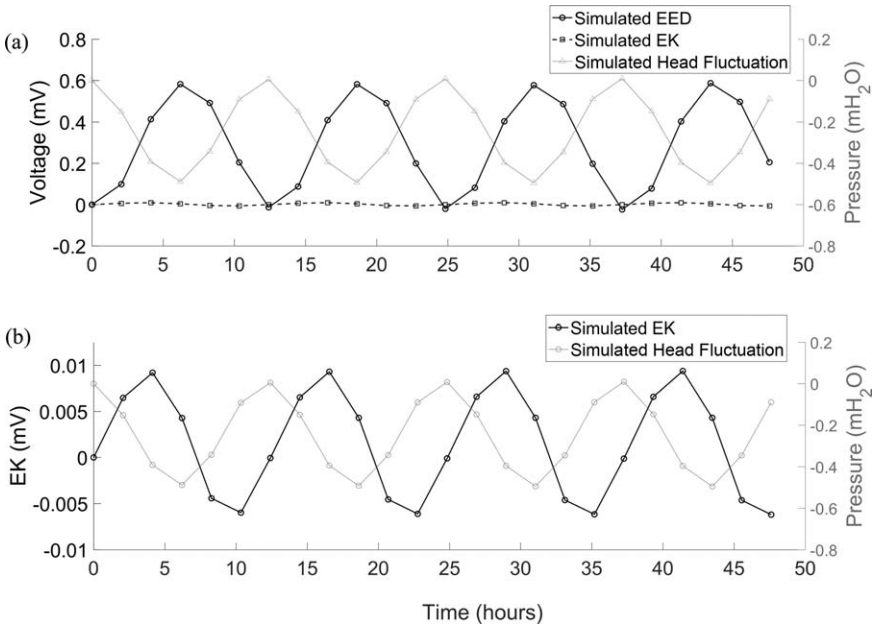


Figure 6. Modeled SP time series results. (a) SP, showing both the EK and EED potential contributions, and normalized pressure fluctuation. (b) EK and normalized pressure fluctuation.

out of phase (Figure 6b). This is investigated further below. The EED potential was the dominant component of tidal SP (Figure 6a) with a magnitude of ca. 600 μV and was caused primarily by fluctuations in the position of the saline front in the fracture zone. Models without the fracture zone showed a tidal SP one order of magnitude smaller. In the best matching model, the SP response in the fracture zone was superimposed on these smaller fluctuations in the matrix. Since EED was anticorrelated with head (ca. 180° out of phase) the SP was also anticorrelated with pressure which is consistent with field observations (Figure 2). Thus, modeling suggests that EED is the dominant component of the observed tidal SP. The modeled SP gradient (Figure 7) also showed a reasonable match to the observed gradient (Figure 3). The SP gradient was also

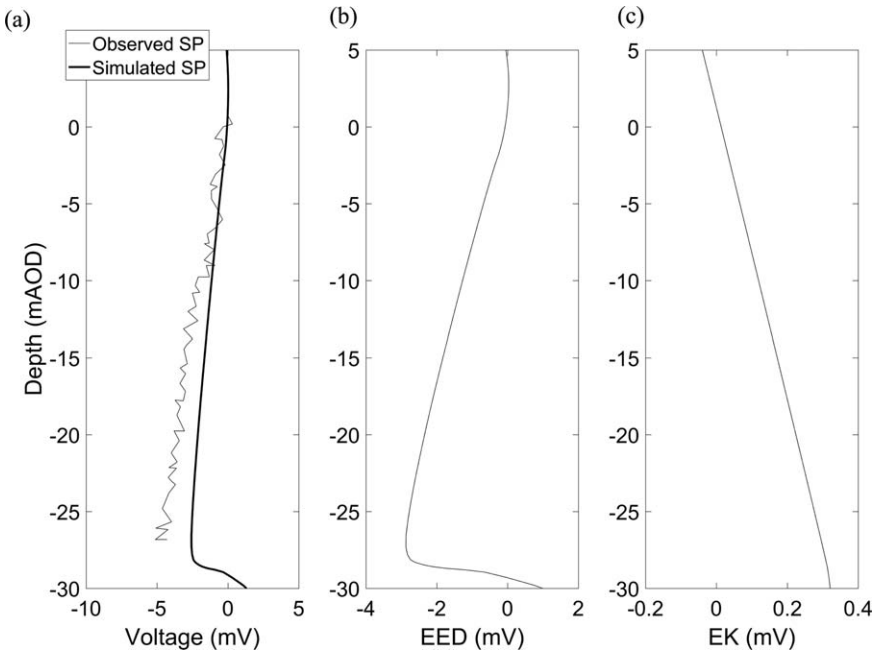


Figure 7. Modeled SP gradient. (a) Simulated (thick black line) and observed SP. (b) EED and (c) EK component of modeled SP.

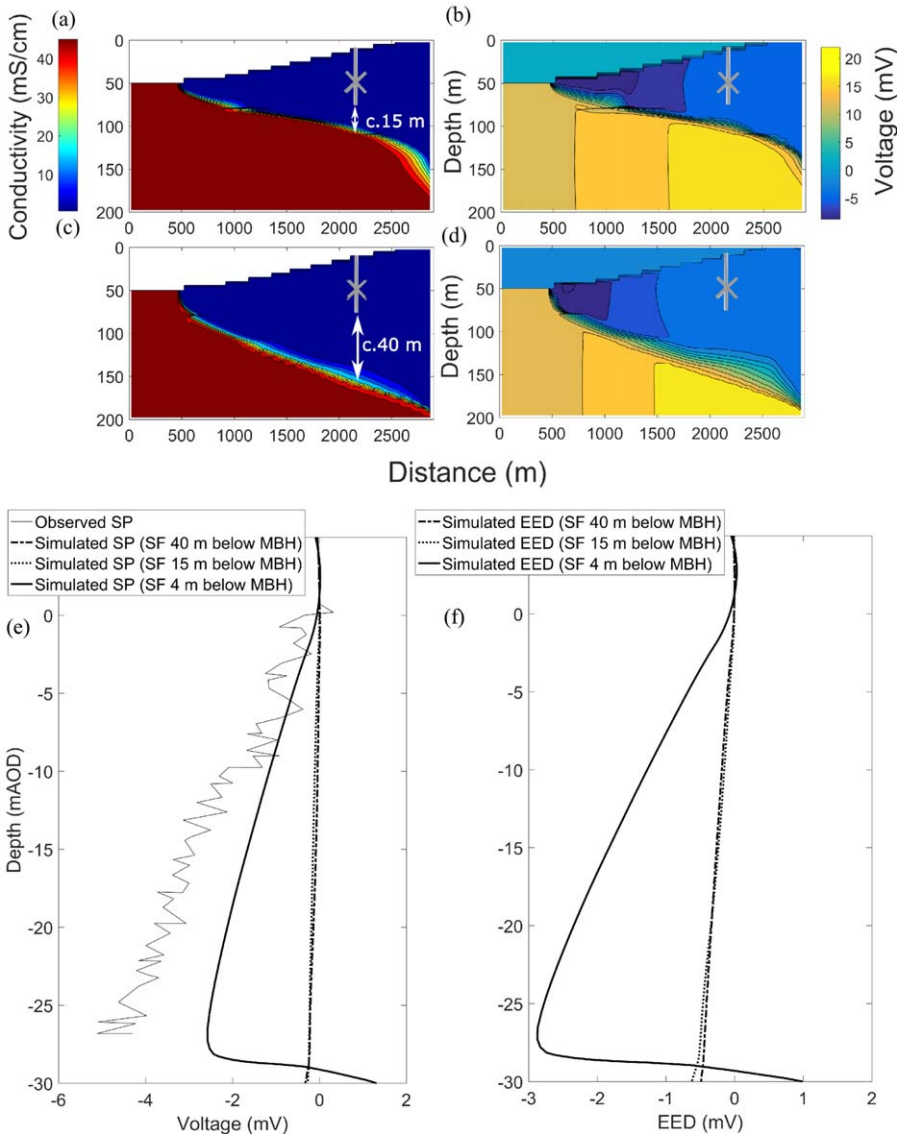


Figure 8. (a and b) FEC and SP for the model with low inland head boundary condition and high bulk permeability at the base. (c and d) FEC and SP for the model with high inland head boundary condition and low bulk permeability at the base. The distance from the base of the borehole to the midpoint of the saline front is indicated for all models and the simulated gradients from these models are shown in Figures 8e and 8f. (e) Change in gradient with increasing distance to the saline front (SF). (f) EED contribution.

dominated by the EED potential, suggesting that the EED potential is the main source mechanism responsible for both the tidal SP response, and the SP gradient, observed in the Saltdean MBH.

3.2.1. Sensitivity Analysis

A simple sensitivity analysis of the electrodynamic model results was conducted by varying the coupling coefficients and, separately, the groundwater rock conductivity. The magnitude of the ocean tidal SP (ca. 0.6 mV in the best fitting model, Figure 6a), varied from ca. 0.3 mV to ca. 1 mV and the change in voltage with depth (ca. 3 mV or ca. 0.1 mV/m in the best fitting model, Figure 7), varied from ca. 1 mV to ca. 5 mV (ca. 0.03 mV/m to ca. 0.16 mV/m) across the ranges shown in Table 1. Importantly the main features, i.e., the gradient and the tidal SP, persisted across all sensitivity models. Moreover, in all models, the EED potential was at least one order of magnitude larger than the EK contribution supporting the conclusion that the EED potential dominates the SP in the Saltdean MBH.

The permeability at depth, which controlled the shape of the saline front and its proximity below the MBH (Figures 8a–8d), had a significant influence on the modeled SP gradient, but negligible impact on the

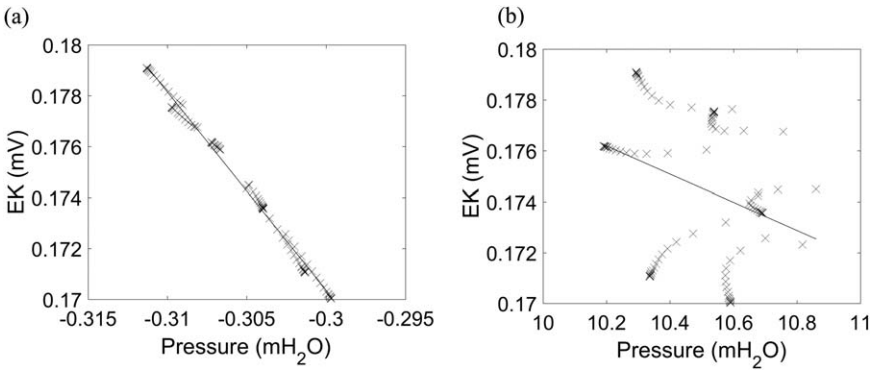


Figure 9. (a) Cross plot of the modeled EK potential versus the pressure difference (above hydrostatic) between the top and bottom of the borehole, equivalent to how the voltages were obtained. The relationship is linear with a coupling coefficient of, -0.779 mV/mH$_2$O. (b) Cross plot of the modeled EK versus the local normalized pressure change measured at a single point.

modeled tidal SP. The tidal EED component was marginally smaller when the depth to the saline front increased (ca. 500 μV compared to ca. 600 μV at ca. 40 m and ca. 4 m from the base of the borehole, respectively). The slight decrease in the EED potential can be explained by the fact that the salinity front, in the bulk rock, was further from the base of the monitoring borehole (ca. 40 m, Figure 8c) and the more mobile part of the saline front, in the fracture zone, was more distant from the borehole (>200 m), consistent with findings reported by Jackson et al. (2012b). The magnitude of the EK potential was unaffected by the position of the saline front. Thus, the tidal signature was not significantly influenced by the permeability structure at depth. Rather, the modeling results suggest that lateral movement of seawater through the fracture zone controls the magnitude of the dominant EED component. However, in models which yielded a steeper saline front, further from the base of the borehole, the SP gradient disappeared (Figures 8e and 8f).

4. Discussion

4.1. Ocean Tidal SP Source Mechanisms

A cross plot of EK versus normalized pressure, from the best fitting model, revealed that the relationship was nonlinear (Figure 9b), because of the phase lag (Figure 6b). The EK coupling coefficient cannot be estimated using the observed head fluctuations (Figures 2b and 2c). Instead, the coupling coefficient must be estimated using the pressure gradient above hydrostatic between the electrodes at the positions of interest, which is very difficult using field data because the pressure difference above hydrostatic is very small. Estimating the coupling coefficient, using the simulated difference in pressure (Figure 9a) between the reference and monitoring position in the model, resulted in a value for the EK coupling coefficient that was greater than the laboratory measured coupling coefficient (Table 1). The larger coupling coefficient is related to the spreading of the current through the 2-D medium (Revil & Linde, 2011). Similarly, the effects of three dimensions in reality further complicate the estimate of the EK contribution directly from the field data.

The modeled EED contribution was ca. 600 μV compared to the ca. 20 μV EK contribution (Figure 6). Evidence for the dominance of the EED component was also demonstrated by Gulamali et al. (2011) and Jackson et al. (2012b) who modeled an intruding water front in an oil reservoir. The importance of the EED potential has also been demonstrated in laboratory sand tank (Ikard et al., 2012; Maineult et al., 2004; Martinez-Pagan et al., 2010) and field tracer experiments (Jougnot et al., 2015; Sandberg et al., 2002).

The source of the EED potential recorded in the Saltdean MBH was the tidally induced movement of the remote saline front through the fracture zone, some distance (ca. 200 m) from the monitoring borehole, combined with smaller tidal fluctuations of the front within the bulk rock (ca. 4 m from the base of the borehole). Similarly, Gulamali et al. (2011), Jackson et al. (2012b), and Jardani et al. (2013) showed that the

presence of fractures and low permeability zones controlled the magnitude of the EED potential. Multiple studies have demonstrated the utility of the SP method for characterizing fracture flow (Hunt & Worthington, 2000; Robert et al., 2011; Roubinet et al., 2016; Suski et al., 2008; Wishart et al., 2008). However, this study is the first to demonstrate remote detection of a fluctuating salinity front in fractured porous media using SP measurements.

4.2. Gradient of SP With Depth

The gradient of the SP with depth was as a ubiquitous feature of the data from the Saltdean MBH. Furthermore, such a gradient was not observed at the inland site or less than 1 km further inland (Figure 3a). The gradient was a result of the close proximity of the saline front to the Saltdean borehole array. Modeling indicated that the gradient was caused by the EED potential (Figure 7). Furthermore, as the modeled saline front became deeper (ca. 15 m and ca. 40 m, respectively, Figures 8a–8d) the SP gradient disappeared (Figures 8e and 8f). In the model that best matched the data, the saline front was only ca. 4 m away from the base of the borehole (Figure 4a). Our results suggest that the presence of an SP gradient with depth indicates that saline water is close to the borehole.

4.3. Impact of Vertical Flow

Conductivity profiles, conducted during saline breakthrough (Figures 3e and 3f), demonstrated that vertical flow occurred within the borehole across the tide. Therefore, there must also have been a vertical head gradient. A rise in head caused the ground water to flow up the borehole and vice versa; therefore, over a tidal cycle the vertical head gradient changed direction. Chalk has a negative EK coupling coefficient (Table 1), so vertical head gradients lead to an EK potential gradient of the opposite direction. Since the vertical head gradient changed direction across the tide, an EK source would also cause the polarity of the SP gradient with depth to change, which was not observed (Figure 3a), confirming the dominance of the EED potential in the observed SP gradient.

A suspected adit (Figure 1d) may have caused the vertical flow observed. As previously discussed, since the properties of the adit are highly uncertain it was not included in the models described above. The adit was simulated in an additional model but, because of these uncertainties, it was not possible to replicate the magnitude of the SP fluctuations accurately. Adit storage was simulated by increasing and calibrating adit porosity, and by calibrating fracture and matrix permeability (to the maximum values in Table 1), to ensure the correct pressure fluctuations in the borehole. When the adit was included in the models a dynamic vertical pressure gradient was induced across the tidal cycle and the EK component did change polarity (Figure 10). The EED component, on the other hand, did not change polarity. In the models that included an adit the vertical change in EK was an order of magnitude too small to explain the SP gradient. Since the borehole was not explicitly simulated in the hydrodynamic models, the water was forced through the bulk rock which is only possible with a large vertical pressure gradient. Thus, it is likely that in the adit model the EK component was overestimated relative to its real contribution. Therefore, the only possible source of the SP gradient with depth, confirmed in all models investigated, was the EED component, caused by the close proximity of the saline front to the borehole.

4.4. Implications for SP Monitoring in Coastal Aquifers

The results presented here suggest that SP can be utilized for remote detection and monitoring of seawater intrusion, including management of pumping regimes to avoid saline breakthrough in coastal boreholes. The SP signal arises primarily as a consequence of the concentration gradient across the saline front while it is remote from the borehole, rather than fluctuations in head at the borehole. Development of an inversion algorithm (e.g., Jardani et al., 2013) could assist in utilizing borehole SP measurements for proactive aquifer management because it would allow the distance of the saline front to be predicted using observed SP signals. Furthermore, by adapting technologies used within the oil and gas industry, SP could be used to provide active inflow control in abstraction boreholes at risk of seawater intrusion (Ijioma & Jackson, 2014). This could be facilitated by automatic SP profiling in abstraction boreholes to identify small changes in the gradient and tidal signatures that indicate changes in the behavior and position of the saline front. Further work, however, would be required to assess the use of SP monitoring in or near abstraction boreholes as the EK component will be larger. A further application of SP monitoring, could be in conjunction with other geophysical techniques (Beaujean et al., 2014; Jardani et al., 2013). Overall, it appears that SP can assist in improving our understanding and management of

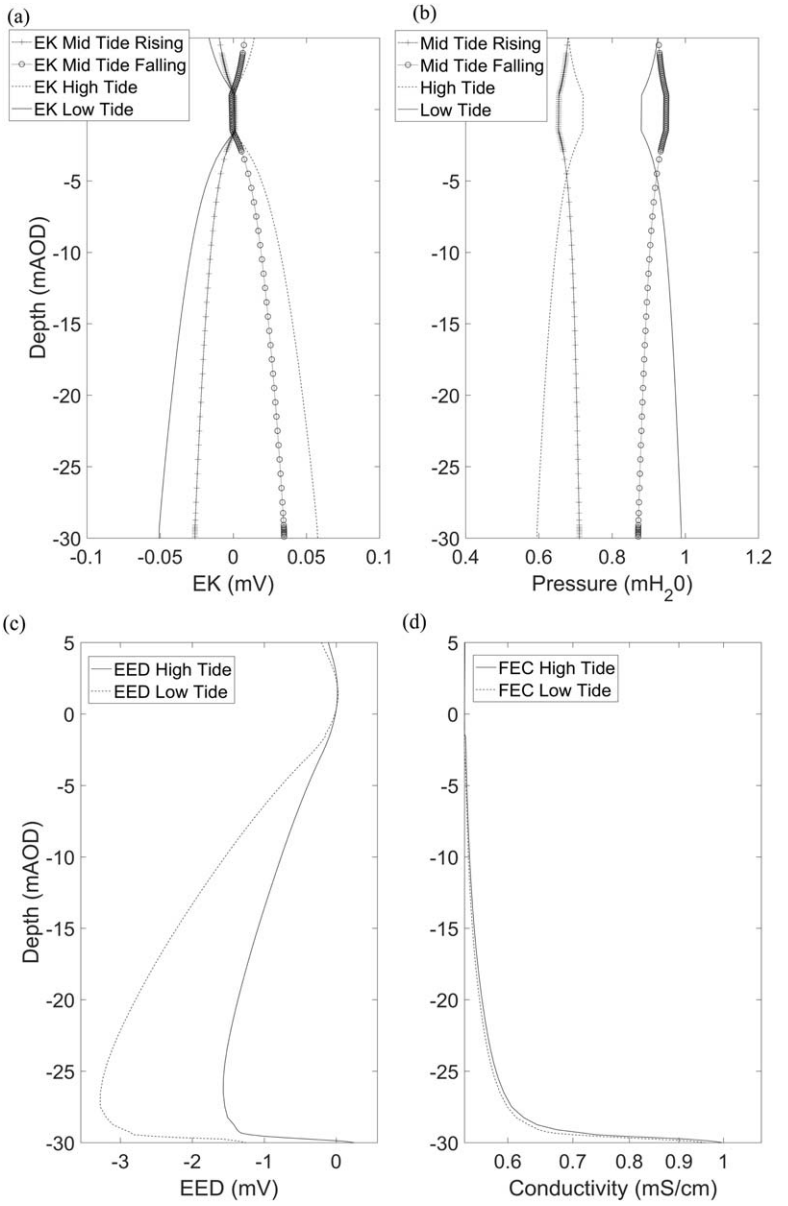


Figure 10. SP results across a tidal cycle from model with an adit, allowing vertical flow to develop. (a) EK, (b) vertical pressure gradient, (c) EED, and (d) FEC with depth.

fractured coastal aquifers. Further work, however, is required to understand how SP could be applied in other aquifer types and in different contexts where fresh groundwater resources may be at risk, including, for example, low-lying coastal deltas or in the vicinity of river estuaries.

5. Conclusions

The numerical models reported here suggest that SP signals observed in the coastal UK Chalk aquifer provide information on the spatial and temporal properties and behavior of a remote saline front during seawater intrusion. The ocean tidal power spectrum observed in the SP was caused by the movement of saline water, some distance away from the monitoring borehole, primarily through a fracture zone near the base of the borehole and superimposed on smaller tidal fluctuations within the bulk rock. The dominance of the electro-exclusion-diffusion (EED) component in the tidal signature implies that the SP recorded in the borehole responded to the movement of a remote saline front long before saline breakthrough occurred at the borehole. Numerical

modeling also confirmed that the EED potential arising from the close proximity of the saline front below the monitoring borehole was responsible for a SP gradient with depth. This effect progressively reduced to zero as the distance from the base of the monitoring borehole to the saline front increased. Therefore, SP measurements were indicative of the position of the remote saline front relative to the monitoring borehole. Thus, SP monitoring can be used to provide early warning of saline breakthrough in coastal boreholes and has the potential to improve management of highly exploited fractured coastal aquifers at risk of seawater intrusion.

Appendix A: Derivation of the EED Potential Coupling Coefficient

The EED coupling coefficient (C_{EED}) used in the models was based on the equation in Jackson (2015). Our modification was based on laboratory measurements (following Leinov and Jackson, 2014) of the EED potential in chalk, which were designed to replicate the concentration gradient between seawater and freshwater during seawater intrusion. All the samples used were natural. Thus, our results (Figure A1) account for the complexity of the groundwater and seawater in the coastal aquifer.

The scaling factor applied in the models (S_{EED}), scales the exclusion potential end-member(V_{EE}), at the concentration ratio between seawater and groundwater, to match the measured EED potential (V_{mEED}, Table 1) (Figure A1):

$$S_{EED} = -\frac{V_{mEED}}{V_{EE}} \tag{A1}$$

We assume in the first instance that the scaling factor, which is conceptually similar to the exclusion-efficiency (Leinov & Jackson, 2014), is constant throughout the model, which may not be the case if local concentration gradients develop, such as between the matrix and the fractures. However, this serves as a reasonable first-order approximation for the processes occurring on the macroscale and across the range of concentrations encountered in the coastal aquifer (Leinov & Jackson, 2014). Given the large error values obtained in the laboratory experiments, their subsequent use in a sensitivity analysis and the fact that there is presently no model that describes the exclusion-diffusion potential of multiionic fluids in a complex charged porous material such as chalk, this approach yields a reasonable first-order approximation of the EED contribution to the overall SP. The EED coupling coefficient was derived as follows (Leinov et al., 2010; Leinov & Jackson, 2014; Jackson, 2015; Revil, 1999):

$$C_{EED} = -\frac{k_b T}{e}(T_+ - T_-) \tag{A2}$$

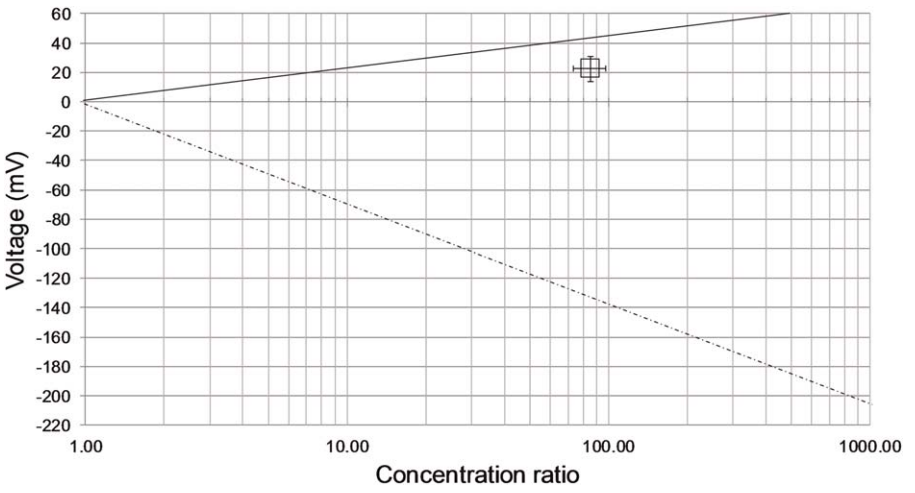


Figure A1. The EED potential (hollow square) measured in the laboratory shown as a function of the concentration ratio. The black line represents the diffusion limit and the dashed line the exclusion limit calculated by Leinov and Jackson (2014).

Here $T_{\pm}$ are the macroscopic Hittorf transport numbers:

$$T_+ + T_- = 1 \tag{A3}$$

For the exclusion potential (V_{EE}) end-member, the macroscopic Hittorf transport number is:

$$T_+ = 1 \tag{A4}$$

Thus, following Leinov and Jackson (2014) and Jackson (2015), and applying the scaling factor, the EED coupling coefficient used in the models was:

$$C_{EED} = -S_{EED}\frac{k_b T}{e} \tag{A5}$$

Acknowledgments
DJM was supported by NERC CASE studentship NE/I018417/1. The authors would also like to thank Southern Water for access to the boreholes at Saltdean and Balsdean. Atkins Global and Southern Water are thanked for funding installation of the equipment and for some additional funding under the NERC studentship. The laboratory components of this work were carried out in the TOTAL Reservoir Physics Laboratory at Imperial College London and their support is gratefully acknowledged. Malcolm Graham, of the Department for Civil and Environmental Engineering at Imperial College London, is also thanked for his contribution to discussions regarding model development and for assisting with data collection from the Balsdean MBH. Four anonymous reviewers are also thanked for their comments which greatly helped to improve the manuscript. The data supporting the conclusions of this work are available through Imperial College London's publication archive (spiral.imperial.ac.uk).

References

Allen, D., Brewerton, L., Coleby, L., Gibbs, B., Lewis, M., Macdonald, A., et al. (1997). *The physical properties of major aquifers in England and Wales* (333 p.). Nottingham, UK: British Geological Survey.

Banks, D., Davies, C., & Davies, W. (1995). The Chalk as a karstic aquifer: Evidence from a tracer test at Stanford Dingley, Berkshire, UK. *Quarterly Journal of Engineering Geology and Hydrogeology*, *28*, S31–S38.

Barker, R. D. (1994). Some hydrogeophysical properties of the Chalk of Humberside and Lincolnshire. *Quarterly Journal of Engineering Geology and Hydrogeology*, *27*, S5–S13.

Beaujean, J., Nguyen, F., Kemna, A., Antonsson, A., & Engesgaard, P. (2014). Calibration of seawater intrusion models: Inverse parameter estimation using surface electrical resistivity tomography and borehole data. *Water Resources Research*, *50*, 6828–6849. https://doi.org/10.1002/2013WR014020

Berkowitz, B., Bear, J., & Braester, C. (1988). Continuum models for contaminant transport in fractured porous formations. *Water Resources Research*, *24*, 1225–1236.

Bloomfield, J. (1996). Characterisation of hydrogeologically significant fracture distributions in the Chalk: An example from the Upper Chalk of Southern England. *Journal of Hydrology*, *184*, 355–379.

Bloomfield, J. P., Brewerton, L. J., & Allen, D. J. (1995). Regional trends in matrix porosity and dry density of the Chalk of England. *Quarterly Journal of Engineering Geology and Hydrogeology*, *28*, S131–S142.

Bristow, R., Mortimore, R., & Wood, C. (1997). Lithostratigraphy for mapping the Chalk of Southern England. *Proceedings of the Geologists' Association*, *108*, 293–315.

Butler, A., Hughes, A., Jackson, C., Ireson, A., Parker, S., Wheater, H., et al. (2012). Advances in modelling groundwater behaviour in chalk catchments. *Geological Society, London, Special Publications*, *364*, 113–127.

Cook, S. J., Fitzpatrick, C. M., Burgess, W. G., Lytton, L., Bishop, P., & Sage, R. (2012). Modelling the influence of solution-enhanced conduits on catchment-scale contaminant transport in the Hertfordshire Chalk aquifer. *Geological Society, London, Special Publications*, *364*, 205–225.

De Franco, R., Biella, G., Tosi, L., Teatini, P., Lozej, A., Chiozzotto, B., et al. G. (2009). Monitoring the saltwater intrusion by time lapse electrical resistivity tomography: The Chioggia Test Site (Venice Lagoon, Italy). *Journal of Applied Geophysics*, *69*, 117–130.

Falgàs, E., Ledo, J., Marcuello, A., & Queralt, P. (2009). Monitoring freshwater-seawater interface dynamics with audiomagnetotelluric data. *Near Surface Geophysics*, *7*(5–6), 391–399.

Glover, P. W., Walker, E., & Jackson, M. D. (2012). Streaming-potential coefficient of reservoir rock: A theoretical model. *Geophysics*, *77*(2), D17–D43.

Gulamali, M. Y., Leinov, E., & Jackson, M. D. (2011). Self-potential anomalies induced by water injection into hydrocarbon reservoirs. *Geophysics*, *76*, F283–F292. https://doi.org/10.1190/1.3596010

Hayashi, M. (2004). Temperature-electrical conductivity relation of water for environmental monitoring and geophysical data inversion. *Environmental Monitoring and Assessment*, *96*, 119–128.

Hunt, C. W., & Worthington, M. H. (2000). Borehole electrokinetic responses in fracture dominated hydraulically conductive zones. *Geophysical Research Letters*, *27*, 1315–1318.

Ijioma, A. A., & Jackson, M. D. (2014). *Closed-loop feedback control of smart wells for production optimisation using downhole measurements of self-potential*. SPE Annual Technical Conference and Exhibition. Society of Petroleum Engineers. Retrieved from https://www.onepetro.org/conference-paper/SPE-170768-MS

Ikard, S. J., Revil, A., Jardani, A., Woodruff, W. F., Parekh, M., & Mooney, M. (2012). Saline pulse test monitoring with the self-potential method to nonintrusively determine the velocity of the pore water in leaking areas of earth dams and embankments. *Water Resources Research*, *48*, W04201. https://doi.org/10.1029/2010WR010247

Ireson, A. M., & Butler, A. P. (2013). A critical assessment of simple recharge models: Application to the UK Chalk. *Hydrology and Earth System Sciences*, *17*(6), 2083–2096.

Jackson, M. D. (2015). 11.09—Tools and techniques: Self-potential methods. In G. Schubert (Ed.), *Treatise on geophysics* (2nd ed.). Oxford, UK: Elsevier.

Jackson, M. D., Butler, A. P., & Vinogradov, J. (2012a). Measurements of spontaneous potential in chalk with application to aquifer characterisation in the Southern UK. *Quarterly Journal of Engineering Geology and Hydrogeology*, *45*, 457–471.

Jackson, M. D., Gulamali, M. Y., Leinov, E., Saunders, J. H., & Vinogradov, J. (2012b). Spontaneous potentials in hydrocarbon reservoirs during waterflooding: Application to water-front monitoring. *SPE Journal*, *17*, 53–69.

Jardani, A., Dupont, J. P., & Revil, A. (2006). Self-potential signals associated with preferential groundwater flow pathways in sinkholes. *Journal of Geophysical Research*, *111*, B09204. https://doi.org/10.1029/2005JB004231

Jardani, A., Revil, A., & Dupont, J. P. (2013). Stochastic joint inversion of hydrogeophysical data for salt tracer test monitoring and hydraulic conductivity imaging. *Advances in Water Resources*, *52*, 62–77.

Jones, H. K., & Robins, N. S. (1999). *The Chalk aquifer of the South Downs*. Nottingham, UK: British Geological Survey.

Jougnot, D., & Linde, N. (2013). Self-potentials in partially saturated media: The importance of explicit modeling of electrode effects. *Vadose Zone Journal*, *12*, 274–294.

Jougnot, D., Linde, N., Haarder, E. B., & Looms, M. C. (2015). Monitoring of saline tracer movement with vertically distributed self-potential measurements at The Hobe Agricultural Test Site, Voulund, Denmark. *Journal of Hydrology*, *521*, 314–327.

Kang, H. J., Cho, I. K., Kim, J. H., Yong, H. H., Song, S. H., & Park, Y. G. (2014). SP monitoring at a sea dike. *Near Surface Geophysics*, *12*, 83–92.

Kullessa, B., Hubbard, B., & Brown, G. H. (2003). Cross-coupled flow modeling of coincident streaming and electrochemical potentials and application to subglacial self-potential data. *Journal of Geophysical Research*, *108*(B8), 2381. https://doi/org/10.1029/2001JB001167

Labregère, D., Delhomme, J. P., & Priestley, A. (2006). Mitigating salt water advance using horizontal wells: Risk based comparison of different approaches. In *First Swim-Swica Joint Saltwater Intrusion Conference, Cagliari, Italy* (pp. 273–280). Swim. Retrieved from http://www.swim-site.nl/pdf/swim19/pages_273_282.pdf; http://www.swim-site.nl/pdf/swim19.html

Leinov, E., & Jackson, M. D. (2014). Experimental measurements of the Sp response to concentration and temperature gradients in sandstones with application to subsurface geophysical monitoring. *Journal of Geophysical Research: Solid Earth*, *119*, 6855–6876. https://doi/org/10.1002/2014JB011249

Leinov, E., Vinogradov, J., & Jackson, M. D. (2010). Salinity dependence of the thermoelectric coupling coefficient in brine-saturated sandstones. *Geophysical Research Letters*, *37*, L23308. https://doi/org/10.1029/2010GL045379

Long, J. C. S., Remer, J. S., Wilson, C. R., & Witherspoon, P. A. (1982). Porous media equivalents for networks of discontinuous fractures. *Water Resources Research*, *18*, 645–658.

MacAllister, D. J., Jackson, M. D., Butler, A. P., & Vinogradov, J. (2016). Tidal influence on self-potential measurements. *Journal of Geophysical Research: Solid Earth*, *121*, 8432–8452. https://doi/org/10.1002/2016JB013376

MacDonald, A. M., & Allen, D. J. (2001). Aquifer properties of the Chalk of England. *Quarterly Journal of Engineering Geology and Hydrogeology*, *34*, 371–384.

Maineult, A., Bernabe, Y., & Ackerer, P. (2004). Electrical response of flow diffusion and advection in a laboratory sand box. *Vadose Zone Journal*, *3*, 1180–1192.

Maineult, A., Bernabé, Y., & Ackerer, P. (2005). Detection of advected concentration and pH fronts from self-potential measurements. *Journal of Geophysical Research*, *110*, B11205. https://doi/org/10.1029/2005JB003824

Maineult, A., Strobach, E., & Renner, J. (2008). Self-potential signals induced by periodic pumping tests. *Journal of Geophysical Research*, *113*, B01203. https://doi/org/10.1029/2007JB005193

Martinez-Pagan, P., Jardani, A., Revil, A., & Haas, A. (2010). Self-potential monitoring of a salt plume. *Geophysics*, *75*, Wa17–Wa25. https://doi/org/10.1190/1.3475533

Mathias, S. A. (2005). *Modelling flow and transport in the Chalk unsaturated zone*. London, UK: University of London.

Maurice, L. D., Atkinson, T. C., Barker, J. A., Bloomfield, J. P., Farrant, A. R., & Williams, A. T. (2006). Karstic behaviour of groundwater in the English Chalk. *Journal of Hydrology*, *330*, 63–70.

Maurice, L. D., Atkinson, T. C., Barker, J. A., Williams, A. T., & Gallagher, A. J. (2012). The nature and distribution of flowing features in a weakly karstified porous limestone aquifer. *Journal of Hydrology*, *438*, 3–15.

Owen, M., & Robinson, V. K. (1978). *Characteristics and yield in fissured chalk* (Thames Groundwater Scheme 33–49). London, UK: Institution of Civil Engineers.

Pezard, P. A., Gautier, S., Le Borgne, T., Legros, B., & Deltombe, J. L. (2009). MuSET: A multiparameter and high precision sensor for downhole spontaneous electrical potential measurements. *Comptes Rendus Geoscience*, *341*(10–11), 957–964. https://doi/org/10.1016/j.crte.2009.07.009

Price, M. (1987). Fluid flow in the Chalk of England. *Geological Society, London, Special Publications*, *34*, 141–156.

Recktenwald, G. (2012). *The control-volume finite-difference approximation to the diffusion equation*. Retrieved from http://web.cecs.pdx.edu/~gerry/class/ME448/notes_2012/pdf/CVFDdiffusion2D.pdf

Revil, A. (1999). Ionic diffusivity electrical conductivity membrane and thermoelectric potentials in colloids and granular porous media: A unified model. *Journal of Colloid and Interface Science*, *212*, 503–522.

Revil, A., Cary, L., Fan, Q., Finizola, A., & Trolard, F. (2005). Self-potential signals associated with preferential ground water flow pathways in a buried paleo-channel. *Geophysical Research Letters*, *32*, L07401. https://doi/org/10.1029/2004GL022124

Revil, A., & Linde, N. (2011). Comment on 'Streaming potential dependence on water-content in Fontainebleau sand' By V. Allegre, L. Jouniaux, F. Lehmann and P. Sailhac. *Geophysical Journal International*, *186*, 113–114.

Revil, A., Trolard, F., Bourrie, G., Castermant, J., Jardani, A., & Mendonca, C. A. (2009). Ionic contribution to the self-potential signals associated with a redox front. *Journal of Contaminant Hydrology*, *109*, 27–39.

Robert, T., Dassargues, A., Brouyère, S., Kaufmann, O., Hallet, V., & Nguyen, F. (2011). Assessing the contribution of electrical resistivity tomography (Ert) and self-potential (Sp) methods for a water well drilling program in fractured/karstified limestones. *Journal of Applied Geophysics*, *75*, 42–53.

Robins, N. S., & Dance, L. T. (2003). A new conceptual groundwater flow system for the Central South Downs Aquifer. *The Journal of Chemical Physics*, *V17*, 111– 116.

Rosas-Carbajal, M., Linde, N., Kalscheuer, T., & Vrugt, J. A. (2013). Two-dimensional probabilistic inversion of plane-wave electromagnetic data: Methodology, model constraints and joint inversion with electrical resistivity data. *Geophysical Journal International*, *196*, 1508–1524.

Roubinet, D., Linde, N., Jougnot, D., & Irving, J. (2016). Streaming potential modeling in fractured rock: Insights into the identification of hydraulically active fractures. *Geophysical Research Letters*, *43*(10), 4937–4944. https://doi.org/10.1002/2016GL068669

Sandberg, S. K., Slater, L. D., & Versteeg, R. (2002). An integrated geophysical investigation of the hydrogeology of an anisotropic unconfined aquifer. *Journal of Hydrology*, *267*, 227–243.

Saunders, J. H., Jackson, M. D., & Pain, C. C. (2008). Fluid flow monitoring in oilfields using downhole measurements of electrokinetic potential. *Geophysics*, *73*, E165–E180.

Schlumberger. (2010). Eclipse reservoir simulator, manual and technical description. ECLIPSE Technical Description, Version 10.

Sill, W. R. (1983). Self-potential modeling from primary flows. *Geophysics*, *48*(1), 76–86.

Singhal, B. B. S., & Gupta, R. P. (2010). *Applied hydrogeology of fractured rocks*. Dordrecht, the Netherlands: Springer.

Suski, B., Ladner, F., Baron, L., Vuataz, F. D., Philippossian, F., & Holliger, K. (2008). Detection and characterization of hydraulically active fractures in a carbonate aquifer: Results from self-potential, temperature and fluid electrical conductivity logging in the Combioula hydrothermal system in the Southwestern Swiss Alps. *Hydrogeology Journal*, *16*, 1319–1328.

Telford, W. M., Geldart, L. P., & Sheriff, R. E. (1990). *Applied Geophysics*. Cambridge, UK: Cambridge University Press.

Van Weert, F., Van Der Gun, J., & Reckman, J. (2009). *Global overview of saline groundwater occurrence and genesis*. Utrectht, the Netherlands: UNESCO and WMO.

Vinogradov, J., Jaafar, M. Z., & Jackson, M. D. (2010). Measurement of streaming potential coupling coefficient in sandstones saturated with natural and artificial brines at high salinity. *Journal of Geophysical Research*, *115*, B12204. http://doi.org/10.1029/2010JB007593

Walton, N. (1989). Electrical conductivity and total dissolved solids—What is their precise relationship? *Desalination*, *72*, 275–292.

Werner, A. D., Bakker, M., Post, V. E. A., Vandenbohede, A., Lu, C., Ataie-Ashtiani, B., et al. (2013). Seawater intrusion processes, investigation and management: Recent advances and future challenges. *Advances in Water Resources*, *51*, 3–26.

Williams, A., Bloomfield, J., Griffiths, K. & Butler, A. (2006). Characterising the vertical variations in hydraulic conductivity within the Chalk aquifer. *Journal of Hydrology*, *330*, 53–62.

Wishart, D. N., Slater, L. D., & Gates, A. E. (2008). Fracture anisotropy characterization in crystalline bedrock using field-scale Azimuthal self potential gradient. *Journal of Hydrology*, *358*, 35–45.

Worthington, S. R. H. (2015). Characteristics of channel networks in unconfined carbonate aquifers. *Geological Society of America Bulletin*, *127*, 759–769.

Worthington, S. R. H., & Ford, D. C. (2009). Self-organized permeability in carbonate aquifers. *Ground Water*, *47*, 326–336.

Erratum

In the originally-published HTML version of this article, Figure 2 incorrectly preceded Table 1. The error has been corrected, and this may be considered the official version of record.